




Design, Manufacture, and Cryogenic Testing of a Linerless Composite Tank for Liquid Hydrogen

Robin Olsson^{1,2}  · Christopher Cameron¹ · Florence Moreau³ · Erik Marklund¹ · Matthias Merzkirch¹ · Jocke Pettersson¹

Received: 21 December 2023 / Accepted: 27 February 2024 / Published online: 18 March 2024
© The Author(s) 2024

Abstract

This paper describes design, manufacture, and testing of a linerless composite vessel for liquid hydrogen, having 0.3 m diameter and 0.9 m length. The vessel consists of a composite cylinder manufactured by wet filament winding of thin-ply composite bands, bonded to titanium end caps produced by additive manufacturing. The aim was to demonstrate the linerless design concept with a thin-ply composite for the cylinder. The investigation is limited to the internal pressure vessel, while real cryogenic tanks also involve an outer vessel containing vacuum for thermal insulation. Thermal stresses dominate during normal operation (4 bar) and the layup was selected for equal hoop strains in the composite cylinder and end caps during filling with liquid hydrogen. Two vessels were tested in 20 cycles, by filling and emptying with liquid nitrogen to 4 bar, without signs of damage or leakage. Subsequently, one vessel was tested until burst at almost 30 bar.

Keywords Burst test · Composite tank · Cryogenic · Filament winding · Liquid hydrogen · Thin plies

1 Introduction and Motivation

Hydrogen is a promising fossil free fuel for future aircraft for tackling climate change and carbon dioxide emissions. The energy content per weight is high, but to minimise the aircraft tank volume the hydrogen must be stored in liquid form at -253 °C (20 K) and 4 bar pressure. Higher temperatures imply an increasing pressure, where the tank becomes partly filled with gas and the pressure must be limited by a controlled “boil-off”. Liquid hydrogen (LH2) has been used in space launchers since the early 1960s, although the research on its use for aerospace begun immediately after WW2 [1]. Obviously, there are many challenges in design of tanks for cryogenic temperatures, i.e. below -153 °C (120 K).

✉ Robin Olsson
robin.olsson@ri.se

¹ RISE Research Institutes of Sweden AB, Box 104, SE-431 22, Mölndal, Sweden

² Dept. of Industrial and Materials Science, Chalmers University of Technology, Göteborg, Sweden

³ Oxeon AB, Företagsgatan 24, SE-504 64 Borås, Sweden

Gas tanks are commonly classified in five types: Type I—metal tanks, Type II—metal tanks hoop-wrapped by composites, Type III—composite tanks with metallic liners, Type IV—composite tanks with non-metallic liners, and Type V—linerless composite tanks. A review of the progress in design of Type V tanks was given in [2] but only a handful of the studies cover storage at cryogenic conditions.

The drawbacks of metal tanks include a higher weight and problems with hydrogen embrittlement, which is a concern for long-term use, particularly in civil aircraft. Carbon fibre polymer composites are the obvious choice for lightweight tanks required, e.g., in aviation. A review of the development of cryogenic composite tanks, with focus on space applications, was provided in [3]. A similar review focused on material issues was recently provided in [4]. The CCTD program by NASA and Boeing, which involved design and testing of 2.4 and 5.5 m diameter launcher tanks, demonstrated weight savings of 33% by replacing aluminium-lithium tank walls by carbon fibre reinforced plastics (CFRP) [5]. Similar tests on a half tank with 0.6 m diameter were performed in Japan [6]. Both these programs were based on use of prepreg material. Currently there are intensive efforts, e.g. within the European programmes “Clean Hydrogen” and “Clean Aviation”, to develop similar tanks for civil aviation.

A challenge with CFRP tanks is that matrix cracking between the fibres normally appears long before the ultimate fibre-controlled failure, which may cause gas leakage and pressure loss. Leakage may be prevented by a metal or polymer liner on the inside of the tank, but the drawbacks are a weight penalty, potential fatigue of the liner due to differences in thermal expansion of the liner and the composite, and risks for separation between the liner and the tank wall. Furthermore, matrix cracking leads to a gradual mechanical degradation of the composite. Linerless tanks for space applications were tested in the previously mentioned programs in USA [5] and Japan [6].

The in-situ strength effect of thin-ply composites can delay, or even prevent, matrix cracking in multidirectional laminates before fibre failure, which allows for linerless (Type V) cryogenic tanks. A theoretical model for the in-situ strength of thin composite plies was presented by Dvorak and Laws [7] and was later extended to shear by Camanho et al. [8]. Existing theory and application to in-house application cases were provided by Olsson [9].

Thin-ply composites have been studied in several research projects, e.g., in Switzerland [10, 11], and in Sweden [12]. Swerea SICOMP (currently a part of RISE) also applied thin-ply composites by the Swedish company Oxeon to a linerless cylindrical composite section for LH2 tanks in the European project CHATT, as described in [13]. Hybrid layups, involving a mix of thin plies and plies of conventional thickness, were used in the CHATT and CCTD projects to reduce costs and increase manufacturing speed.

Filament winding, most commonly using an inline resin bath or a rotating drum for wetting of the fibres, is a well-established commercial method for producing pressure vessels in composite materials. One drawback of the wet-winding process is, however, limitations with regards to design of the end cap-section of the vessel.

The current paper describes design, manufacture, and testing of a linerless composite vessel for liquid hydrogen within the Swedish project “LH2-Tanks”, as shown in Fig. 1. The long-term aim is development of lightweight composite tanks for liquid hydrogen in future commercial aircraft. The aim of the project was to extend the work of RISE in CHATT by a thorough material characterisation at room temperature and at -253 °C, to use the data to design a vessel, and to demonstrate the linerless design concept for the cylindrical part in a complete vessel under realistic test conditions. In contrast to the cylindrical section in CHATT it involves real end caps (rather than plugs) and is tested under internal pressure in cyclical loading and to burst.

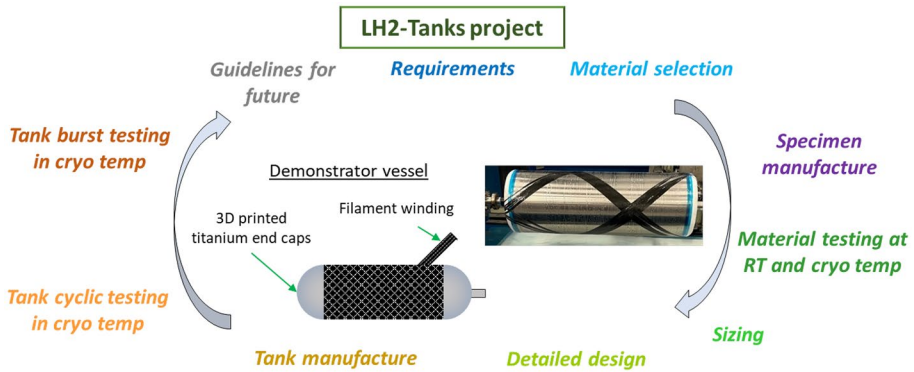


Fig. 1 Overview of the LH2-Tanks project

The project is limited to the internal pressure vessel, while real cryogenic tanks also include an outer vessel containing an intermediate space with vacuum for thermal insulation. Other tasks of the project have been performed by the SME:s Oxeon (material manufacturer and developer) and Konvegas (studies for future production of gas tanks for cars), Chalmers University (hydrogen diffusion and initial design studies), and Linköping University (fatigue testing and modelling).

The vessel involves a linerless composite cylinder manufactured by wet filament winding of thin-ply composite bands, which is bonded to two titanium end caps (domes) produced by additive manufacturing.

2 Design Requirements and Material

2.1 Design Requirements

Liquid hydrogen can be stored between $-253\text{ }^{\circ}\text{C}$ (20 K) at 1 bar and the critical point $-240\text{ }^{\circ}\text{C}$ (33 K) at 13 bar but is typically stored at about 4–5 bar. The maximum tank pressure is managed by safety valves allowing a controlled boil-off at, e.g., 10 bar. In the current case the aim is a tank for future civil aircraft, which implies at least 3 fuelling cycles a day for 20 years, i.e., over 20000 cycles. During these cycles the tank will normally not be fully emptied or heated by more than $110\text{ }^{\circ}\text{C}$. Complete emptying and heating will only take place during the annual service overhauls, i.e., about 20 times during the lifetime. Additional requirements may include inertial loads during flight, thermal gradients in the tank, and potential pressure bursts during fuelling, but such effects were not considered in the current design.

2.2 Material and Material Data

The material for the composite cylinder consisted of 20 mm wide and 0.050 mm thick TeXtreme[®] thin ply unidirectional (UD) bands manufactured by Oxeon through a spread-tow technique, but the winding of the cylinder resulted in an actual ply thickness of about 0.10 mm after manufacture. The bands consist of Pyrofil[™] TR50S carbon fibres with an

epoxy binder for dimensional stability, which during the wet-winding were impregnated with a special epoxy suited for cryogenic applications.

The hydrogen permeability of the composite before and after mechanical loading was examined in a separate study [14]. Tests were only done in the interval $+5\text{ }^{\circ}\text{C}$ to $+45\text{ }^{\circ}\text{C}$, but confirmed the expected decreasing diffusion rate with temperature, and that leak rates would be well below required values for cryogenic tanks.

The material data for the composite were determined by testing filament wound, almost unidirectional (UD), coupons with $\pm 0.6^{\circ}$ layup at room temperature (RT) and at $-253\text{ }^{\circ}\text{C}$ (20 K), as described by Merzkirch et al. [15]. Coefficients of thermal expansion (CTE) were also determined for a range of intermediate temperatures. Both the composite cylinder and the UD coupons were made by wet filament winding and had a void volume fraction of less than 2%. Figure 2 gives a comparison of cross-sections of the UD coupons and a laminated cylinder of the vessel.

The fibre volume fraction (FVF) in the angle-ply composite cylinders was found to be 51%, i.e., somewhat lower than the 57% in the UD test coupons. For this reason, the material data obtained from UD test coupons with $\text{FVF}=57\%$ need to be corrected to $\text{FVF}=51\%$ before they can be used in the tank design. The corrections for FVF were done using analytical micromechanics equations and theory for in-situ strength, as described in [15]. Furthermore, the in-situ strengths had to be adjusted to the actual ply thickness in the cylinder, which was 0.10 mm. Table 1 lists estimated elastic properties and strengths of the plies with $\text{FVF}=51\%$ at two relevant test temperatures and *average* values during cooling from $+94\text{ }^{\circ}\text{C}$ to these temperatures. The temperature $-100\text{ }^{\circ}\text{C}$ corresponds to the measured temperature in the vessel at final burst. Since the fracture toughness at cryogenic temperatures was not measured, values of $G_{Ic} = 200\text{ J/m}^2$ and $G_{IIc} = 620\text{ J/m}^2$ were assumed (approximately 20% and 40% lower than measured at RT).

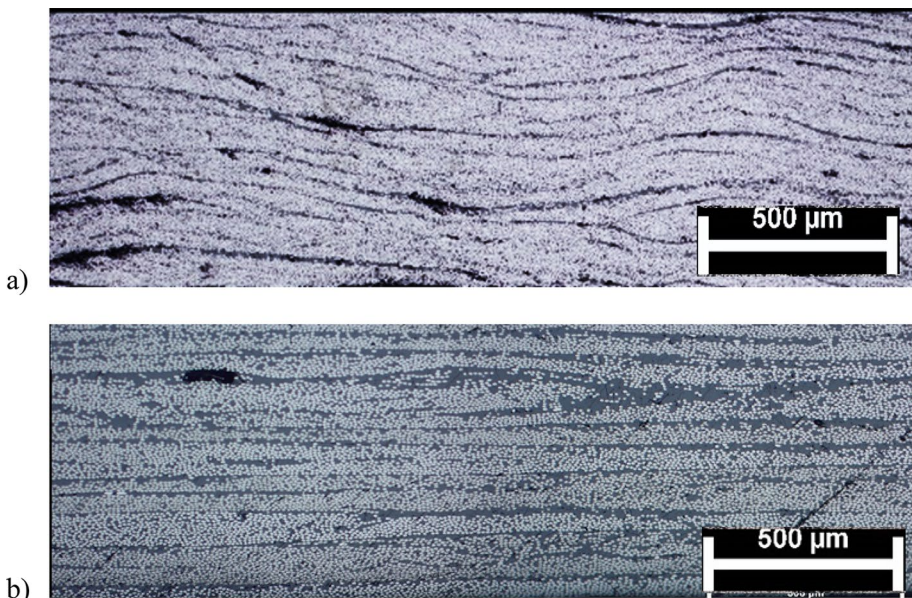


Fig. 2 Microscopy of **a** a flat $\pm 0.6^{\circ}$ (nominally UD) laminate and **b** cylindrical $\pm 40^{\circ}$ laminate

Table 1 Elastic properties and strengths of 0.1 mm thick plies with FVF=51% used for modelling

Temperature	Poisson's ratio ν_{12}	Stiffness [GPa]			CTE ($T_{ref}=94\text{ }^{\circ}\text{C}$) [$10^{-6}/^{\circ}\text{C}$]		Strength [MPa] X_t	In-situ strength surface/embedded single ply [MPa]	
		E_1	E_2	G_{12}	α_1	α_2		Y_{IS}	S_{IS}
+94 °C to -253 °C	0.31	119	9.0	4.1	0.4	27.3	-	-	-
-253 °C	0.31	120	10.2	4.8	-	-	1937	114/161	195/275
+94 °C to -100 °C	0.31	119	8.3	3.7	0.4	33.8	-	-	-
-100 °C	0.31	119	9.1	4.2	-	-	1931	108/152	182/258

Note that the CTEs only are given as average values during cooling, as these values were used to determine the thermal strains. Similarly, the strengths are only given at the final temperature after cooling, as these values were used to determine failure under addition of the applied pressure.

3M Scotch-Weld epoxy adhesive 2216 B/A gray was used in the adhesive joint. Assuming $\nu=0.35$ an average Young's modulus for thermal stress analysis was estimated from the shear modulus given by the manufacturer [16] for the range +24 °C to -100 °C, which was extrapolated to -253 °C.

The metal components were made by additive manufacturing with a titanium Ti-6Al-4V alloy.

3 Design Procedure

3.1 Design Concept

At an early stage it was decided to manufacture the vessel by combining a composite cylinder made by filament winding with metal end caps (domes) made by additive manufacturing (AM). The choice of filament winding was based on extensive previous experience of this technique for producing high quality cylinders from thin-ply composites. Metal end caps produced by AM were chosen to make sure that the weak part was not the end caps, and considering the complex doubly curved shape, the need to include threaded connections for pipes, the small number of vessels, and the fact that a uniform thickness and isotropic in-plane properties are optimal for hemispheres under internal pressure. Obviously, this is hard to achieve using a filament winding procedure. Titanium was selected due to its low density and a CTE closer to composite laminates than e.g., aluminium and steel. This design requires a bonded joint between the composite cylinder and the titanium end caps.

Initial analysis demonstrated that the thermal stresses dominated in the composite cylinder, while the stresses due to the internal pressure were negligible at the normal operational pressure (4–10 bar). Furthermore, the adhesive joint might be a weak link. For this reason, the length of the adhesive joint was adapted to accommodate a 10 bar pressure with the apparent (average) shear strength in lap shear tests performed after ten dipping cycles in liquid nitrogen (LN2). To minimise peel stresses in the adhesive joint the layup of the composite cylinder was focused on matching the thermal hoop strains of the composite cylinder and the metal end caps, while preventing matrix cracking in the laminate. An outer support

ring in titanium was also added to prevent peeling and to double the path for hydrogen leakage in case of cracking in the adhesive joint.

3.2 Preliminary Design

To reduce the mismatch in thermal strains between the titanium end-caps and the composite tube, it was decided to use a winding angle that minimises the diameter change between the two materials, from bonding at +60 °C down to cryogenic temperature at -253 °C. Therefore, the aim was to select a winding angle that matches the hoop CTE of the composite with the CTE of titanium (Grade 5) in this temperature range. For this thin-walled cylinder, classical laminate theory (CLT) could be used to estimate the axial and hoop thermal expansion coefficients. For a symmetric laminate, in which there is no coupling between in-plane forces and bending moments, the free thermal strains are given by $\{\varepsilon\}_0^{th} = [A]^{-1}\{N\}^{th}$, where $[A]$ is the laminate extensional stiffness matrix and $\{N\}^{th}$ are the thermal forces. If the CTEs of the UD ply are known the effective CTEs of the laminate are given by:

$$\{\alpha\}_{lam} = \{\varepsilon\}_0^{th} / \Delta T \quad (1)$$

Measurements of α_1 and α_2 for the current material, but with $v_f = 57\%$, were given in [15]. A micromechanics methodology for how to correct ply stiffness and CTEs to other temperatures and fibre volume fractions was also given. The same methodology was used here to calculate average CTEs in the range from +60 °C to -253 °C for a UD ply having $v_f = 51\%$, assuming that the matrix modulus and the CTEs of the matrix and the fibres vary linearly with temperature and that it can be extended to temperatures above RT. Then, using CLT and Eq. (1) the axial and hoop CTE were calculated for different $\pm\theta$ winding angles, as shown in Fig. 3a. The mean CTE of titanium in this temperature range ($\alpha_{Ti} = 6.610^{-6}/^{\circ}\text{C}$) was estimated from the formula in [17]. Figure 3a shows that the hoop CTE is approximately equal to that of titanium for a winding angle of 41°, which was selected as primary candidate for further design. The resulting CTEs were $\alpha_H = 6.410^{-6}/^{\circ}\text{C}$ in the hoop direction and $\alpha_A = -0.310^{-6}/^{\circ}\text{C}$ in the axial direction.

A section from a cylinder from the first 41° winding trials was used to measure the CTE in axial and hoop directions, see Fig. 3b. Two thermocouples close to the test object were used to monitor temperature. Temperature range was from RT to -150 °C

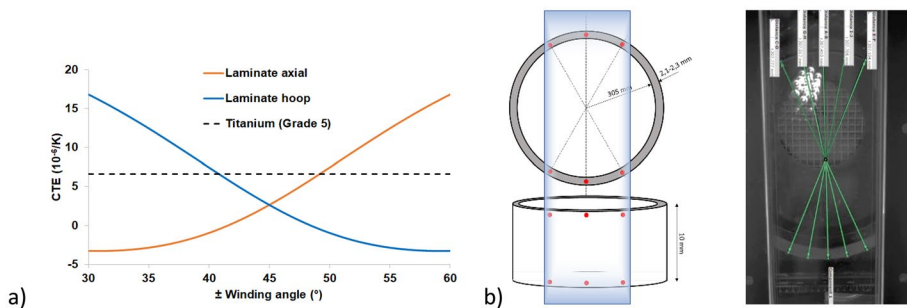


Fig. 3 **a** Theoretically calculated CTEs of a composite cylinder depending on \pm winding angle. **b** Measurement of axial and ring deformation using DIC

with a cooling rate of 2 °C/min. Five evenly spaced measurement points in both directions, at locations that could fit within the climate chamber window, were used to measure the dimensional changes with DIC. The average CTEs from these measurements were $\alpha_H = 5.710^{-6}/^{\circ}\text{C}$ and $\alpha_A = 1.310^{-6}/^{\circ}\text{C}$. The results do not represent the entire section but are quite close to the predicted values, although the temperature range is different, and the tested ring section had a slightly different fibre volume fraction ($v_f = 53.9\%$ as determined by matrix “burn-off”).

In the next step it was checked that the plies at the chosen winding angle were able to withstand the thermal stresses in combination with a relative pressure of 10 bar without cracking or failing. For a thin-walled cylinder with radius R and wall thickness h , under an internal relative pressure p , both hoop σ_H and axial stress σ_A are present:

$$\sigma_H = pR/h, \quad \sigma_A = \sigma_H/2 \quad (2)$$

At this design stage the expectation was to use a 2 mm thick cylinder with 305 mm inner diameter, having a total of 20 “plies” with 0.1 mm thickness. The maximum stress criterion and a quadratic criterion for matrix cracking were applied on ply level to predict the failure pressure (either by fibre failure or by matrix cracking). For the maximum stress criterion failure occurs when *any* of the stress components reaches its strength limit:

$$\frac{\sigma_1}{X_t} = 1, \quad \frac{\sigma_2}{Y_{IS}} = 1 \text{ or } \frac{|\tau_{12}|}{S_{IS}} = 1 \quad (3)$$

For the quadratic criterion matrix failure occurs when:

$$\frac{\sigma_2^2}{Y_{IS}^2} + \frac{\tau_{12}^2}{S_{IS}^2} = 1 \quad (4)$$

Here the quadratic criterion is also combined with the maximum stress criterion in fibre direction. Due to the internal pressure, a linearly varying compressive stress is present through the thickness of the cylinder wall, but this stress component is much smaller than the in-plane stresses and was neglected. The quadratic criterion is more conservative than the maximum stress criterion due to the interaction between transverse tension and shear stress.

For the current material onset $T_g = 94$ °C was measured using DMA [15]. Here it is used as approximated stress-free temperature and thus as reference temperature for thermal stress calculations in the composite. The thermomechanical loading is applied in two steps: First the thermal load is applied using the calculated thermomechanical ply properties shown in Table 1. Secondly, the pressure difference is applied using the calculated material properties at -253 °C, and failure pressure predicted using both failure criteria.

Figure 4a shows the calculated thermal stresses for the innermost surface ply depending on \pm winding angle. Actually, the stresses are the same for all plies when using CLT, except that the shear stress changes sign for + or - angle. The highest thermally induced transverse stress is about 75 MPa for $\pm 45^\circ$ winding angle. Figure 4b shows the predicted failure pressure. As expected, the quadratic failure criterion is more conservative than the maximum stress failure criterion. For all winding angles the dominating failure mode is transverse tensile failure, i.e., matrix cracks running parallel to the fibres. However, reducing the ply thickness, may shift the failure mode to fibre failure for certain angles. The highest fibre stress at failure is found for angles 52° – 54° depending on the criterion used and if it is a surface ply or embedded ply. Clearly, winding at an angle 52° – 54° would be optimum

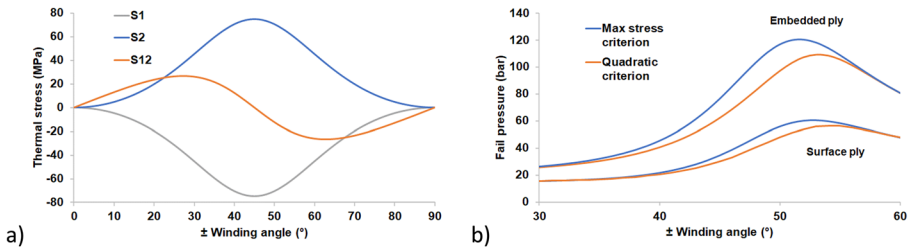


Fig. 4 **a** Thermal stresses for the innermost surface ply from 94 °C to -253 °C. **b** Calculated failure pressure (first ply failure)

from a mechanical perspective, but the aim here is to minimise the thermal mismatch to titanium, while still being on the safe side with a design pressure of 10 bar. For $\pm 41^\circ$ winding it is predicted that the surface plies will crack at a pressure of 22 bar and the embedded plies at 44 bar. Obviously, this analysis does not consider the micro/mesostructure of the plies and that cracks in surface plies may cause premature failure of embedded plies.

3.3 Detailed Design

3.3.1 FE Modelling Approach

Estimation of the mechanical stresses due to the combined thermal loading and internal pressure required the use of FE analysis to determine the necessary thickness of the cylinder wall, and to examine in detail the response of the bonded joint under the combined loading.

It is well established within the literature, [18, 19], that composite materials have varying properties depending upon the temperature at which they are measured. For the current work, it was decided that accurate prediction of the structural response would require changing material properties with temperature. To achieve this, a user defined material model (UMAT) was developed in Fortran for use with Abaqus 2019.

The UMAT was a linear elastic temperature dependent material model, where the properties were dictated by the applied temperature on the material. The simplified model assumed one set of linear elastic material properties from the initial curing temperature (i.e., stress-free temperature) down to a defined lower-limit temperature, and a second set of material properties below this temperature. This UMAT was used to evaluate the initial stress state due to the thermal load, which was then used as the “base state” for the pressure loading of the vessel at cryogenic temperatures.

Two levels of detail were required for the overall design. Firstly, a global model of the vessel was used to understand the effects of thermal strains on the doubly curved end-caps and the cylinder. Secondly, a refined model was used to resolve the detailed stress state at the bonded joint between the composite tube and the titanium end caps.

3.3.2 Global FE Model

A partial model of the vessel was created, involving a hemispherical titanium end cap, a 100 mm long segment of the composite cylinder and an outer support ring in titanium. The cylinder segment was selected sufficiently long to achieve steady state stresses, assuming symmetry at the end of the cylindrical portion of the vessel. For the analysis, a temperature

load was applied to the entire structure corresponding to the temperature change from the curing temperature down to liquid hydrogen ($-253\text{ }^{\circ}\text{C}$). In the next step of the analysis, a pressure load corresponding to 10 bar was applied to the inner surfaces of the vessel.

The layup of the composite cylinder was selected to match the CTE in the hoop direction to the titanium parts, which resulted in a very large CTE in the axial direction of the cylinder. Obviously, the large temperature change from the stress-free state to $-250\text{ }^{\circ}\text{C}$ caused a correspondingly large lengthwise shrinkage of the vessel.

The combination of thermal contraction in the axial and circumferential direction of the vessel resulted in very high stress levels within the adhesive bond between the end cap end, the composite tube, and the outer reinforcement ring. The von Mises stress in the adhesive layer at 10 bar internal pressure exceeded 150 MPa, which was anticipated to exceed the strength of the adhesive. For this reason, a detailed model was done to further refine the stress state at the bond line and within the surrounding structure of the vessel. Both models used homogenised properties of the laminate and did not model plies individually.

The FE analysis indicated a safety factor of 7.5 for plastic deformation of the titanium Ti-6Al-4V alloy, which has a yield stress of 880 MPa. Furthermore, it should be stressed that the sole purpose of the end caps was to allow “proof-of-concept” for a linerless composite cylinder under realistic biaxial stress with internal pressure. Thus, the metal end caps were not optimised for minimum weight, but to allow convenient manufacture with the available 3D-printing equipment.

3.3.3 Refined FE Model

Using the response of the global model, a submodel was created to study the local stress state within the bonded joint area of the vessel, Fig. 5, which was anticipated to be the most likely area for failure. The geometry of the sub-model was taken from the global model, and the mesh was refined considerably. Displacements of the global model were prescribed as boundary conditions for the outer edges of the refined model, according to standard practices of submodel simulation described in the Abaqus documentation.

The cross section of the connection was refined to model the end cap, outer ring, tubular section, and the adhesive layer with 3D solid elements. Both the composite section of length 100 mm, and the adhesive layer used a two-state linear elastic material model with properties selected based on the applied temperature. These sections were modelled with multiple elements through the thickness. The same pressure and temperature loads were

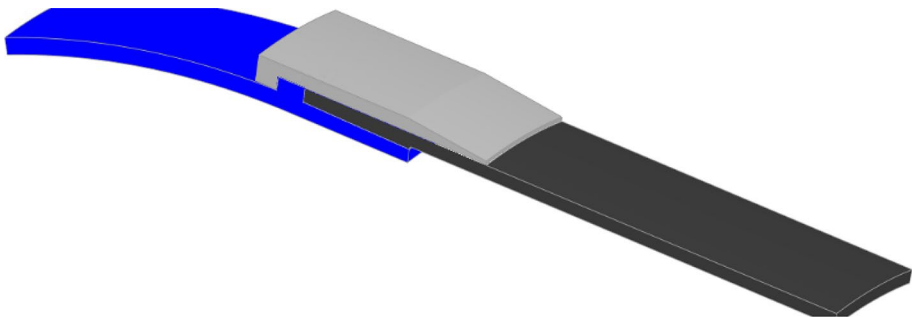


Fig. 5 The submodel of the joint section

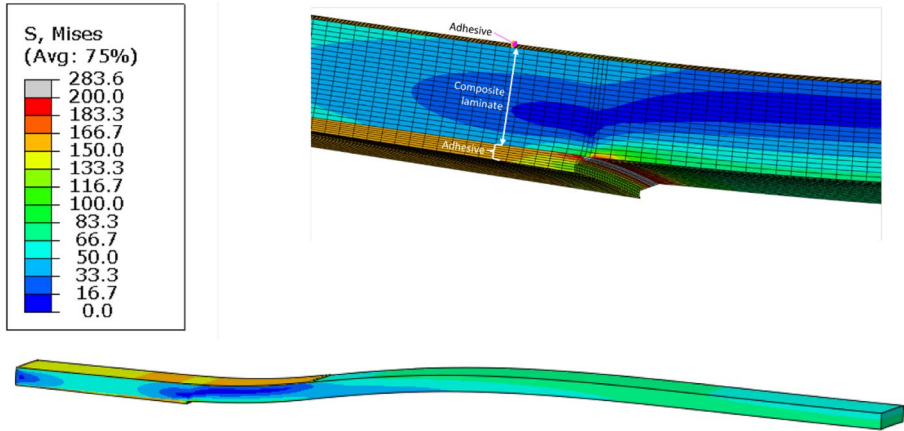


Fig. 6 von Mises stress in the overall joint area, with a close up of the adhesive layer in the transition zone

applied to the refined model. A close up of the geometry around the joint can be seen in Fig. 6. Deformations are shown with a scale factor of 10 for visualisation purposes.

To get an accurate picture of the stresses across the joint and in the composite, it was necessary to take nodal data from a path along the middle of the model to avoid the effects of the transformation of displacements from the global model to the submodel.

Detailed results of the stress states in the bond area are given in Figs. 6, 7, 8 and 9 and explained below.

Figure 6 shows that the stresses within the bond are significant, with a peak at the end of the joint end and levelling off to approximately 150 MPa. This model should not be considered as a reliable prediction of failure but as a hot spot analysis, identifying the adhesive joint as a potentially weak link of the design. Polymers have significantly

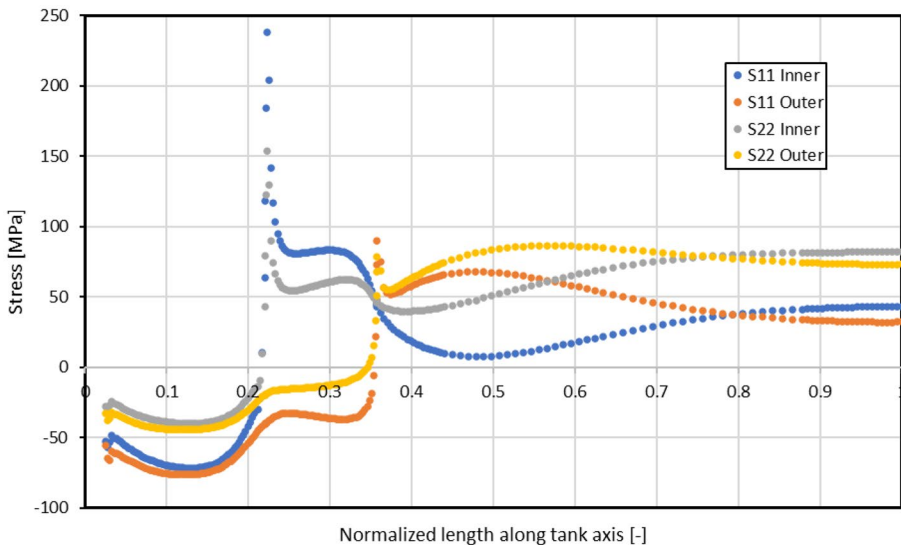


Fig. 7 Axial(S11) and Hoop(S22) stress in cylinder wall from end cap end towards symmetry plane

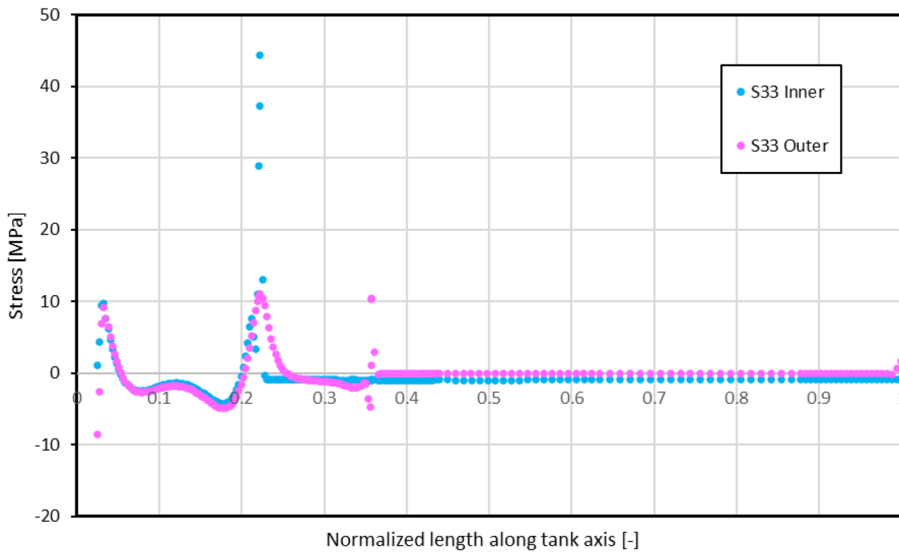


Fig. 8 Out-of-plane stress at surface of composite cylinder wall along longitudinal axis

higher strength in compression than in tension, and a reliable failure prediction requires a pressure sensitive failure criterion, e.g., by Raghava, and access to material data of the adhesive both in tension and compression at cryogenic temperature. Furthermore, the predicted peak stresses are highly dependent on the assumed radius at the end of the joint, and also to some extent on the mesh density. Finally, the current model was linear elastic for each given temperature. In reality stress concentrations will be relieved by local yielding or damage, which requires a nonlinear material model.

Figure 7 shows the axial and hoop homogenised stresses as taken from the inside and outside faces of the composite section along its axis, using normalized distance from the innermost joint area to the assumed symmetry plane at the right end of the tube. Figure 8 shows the out-of-plane stress along the same path as the previous figure.

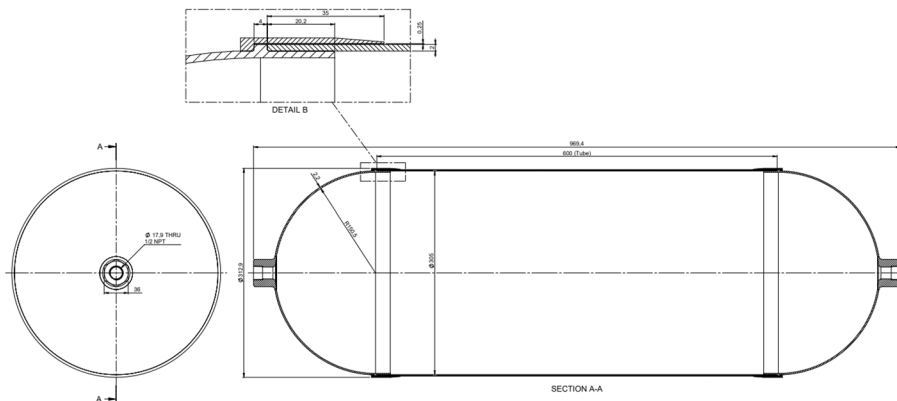


Fig. 9 Overview assembly drawing

In the first section ($x=0-0.23$) the composite tube is constrained between the end cap and the outer support ring, and an overall compressive stress state is observed. In the second section ($x=0.23-0.35$), the end cap has been terminated and the outer ring is tapering off. In the final section ($x=0.35-1.0$) the stresses approach the steady state values in a long cylinder.

Significant tensile stresses are only observed at the end of the end cap. Furthermore, the bending stresses (as defined by the difference in stresses on the inside and outside of the wall) are relatively moderate, except in the axial direction of the tube. Stresses are very high in the bonded joint, both on the inside and outside of the tube despite careful attention to detail in reducing jumps in stiffness and trying to match CTE between the composite and the metallic parts. This high stress level is primarily due to thermal loading. As an example, a temperature reduction from $+20\text{ }^{\circ}\text{C}$ to $-253\text{ }^{\circ}\text{C}$ increases the stress in the axial direction of the vessel by about 100 MPa. It may be possible to lower this stress slightly by using a system with lower cure temperature, given that the stress-free state in this analysis was assumed to be $+40\text{ }^{\circ}\text{C}$.

It appears that the metallic parts and the composite wall of the chosen materials should be able to accommodate the predicted stresses.

The bond area is the most likely area to fail. Out-of-plane stresses higher than 20 MPa are observed, which could very well lead to peel failure of the joint, but this was difficult to predict as no cryogenic data for the adhesive is known. Given the large jumps in stress at the ends of the bonds to the titanium parts, it would be anticipated that any failure of the bond would initiate here and potentially grow through the bonded area. Exactly where the crack would initiate and how it would propagate could not be predicted given the limited data for the adhesive. It should, however, also be noted that crack growth in the adhesive joint would have to occur into the region $x < 0.23$, where the out-of-plane stresses are moderate or negative and where the in-plane stresses are compressive.

4 Manufacture

4.1 Design Concept for Manufacture and Assembly

An assembly drawing of the complete vessel is shown in Fig. 9. The vessel consists of a central composite cylinder bonded to two titanium end caps. An outer support ring in titanium was pushed over the end-cap and bonded to the composite cylinder, as illustrated in the subfigure “Detail B”. The vessel has an interior volume of 58 L, a maximum outer diameter of 313 mm, and a total length 969 mm, including threaded nipples.

The geometries consist of a tube and end caps, both with thicknesses of about 2 mm. The inner diameter of the tube is 305 mm. The thickness of a bond-line for a structural adhesive is typically 0.1–0.2 mm for good performance. To achieve necessary tolerances of the tube and end-cap diameters, leaving a correct gap of 0.1–0.2 mm for the bond line, is a challenge due to the rather thin-walled components in relation to the diameter. The main reason is that the thin walls do not allow much machining until the wall thickness is affected significantly. The chosen solution to meet tolerances was to let the most consistent measurement of the components set the baseline. In this case, the inner diameter of the composite tube, was used as manufactured, without machining. The end-cap, the outer ring and the outer diameter of the composite tube were manufactured with excess material to be machined to achieve correct gaps for the inner and outer bond lines.

By adding a stop ring on the endcap outer surface, shown in “detail B”, Fig. 9, the assembly is positioned lengthwise without need for external fixture while bonding the parts.

Two identical demonstrator vessels were manufactured and tested, to give some indication of variations in manufacturing quality, and to reduce the risk of invalid tests due to a single manufacturing flaw.

4.2 Manufacture of the Composite Cylinder

Wet filament winding was used for production of the tubes. The greatest challenges were winding of thin layers at a relatively low winding angle and to achieve a low porosity and high fibre volume content. The requirement to keep a consistent layup with $\pm 41^\circ$ was met by using a spread-tow band width of 20 mm. Disposable spiked end-domes were fitted to each end of the mandrel to minimise sliding of the spread tow after turning. Figure 10a shows a part of the cylinder with a spiked end dome at the right end. To achieve the required fibre volume fraction and low porosity, dry compression layers of a peel-ply were wound on top of the wet wound tube, Fig. 10b. As final layer, a dry hoop wound carbon fibre layer, set at high fibre tension, was used to control the compaction and bleed-out of excessive resin prior to curing. The compaction of the wet wound tube is shown in Fig. 10c. After curing under rotation at elevated temperature, the dry compaction layers and the disposable end caps were removed. The tube was then removed from the mandrel and cut to desired length.

After completed manufacture the geometry of the composite cylinders was measured using the optical Atos Q 8M system by GOM GmbH and the software GOM Inspect. An example of the measurements is shown in Fig. 11. The measurements were used as input for prescribed dimensions from the additive manufacture, with the aim to achieve the tolerances required for assembly and bonding with minimised machining.

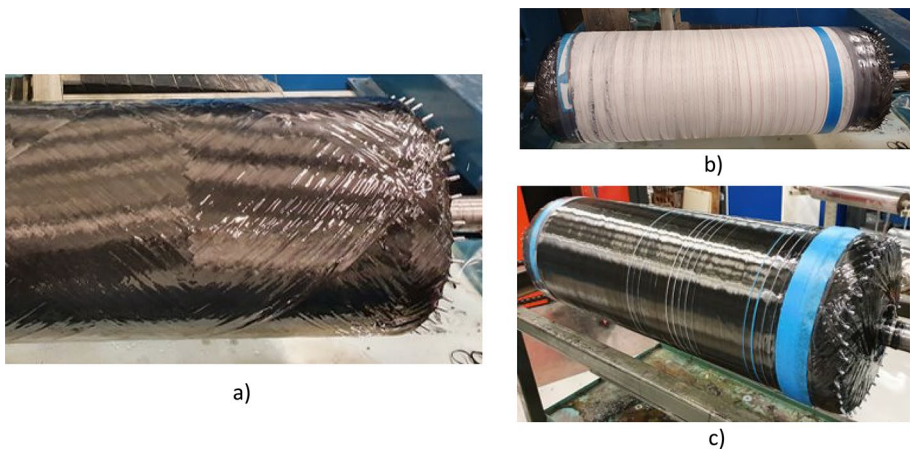


Fig. 10 Spiked end domes on each end of mandrel prevents the fibres from sliding after turning

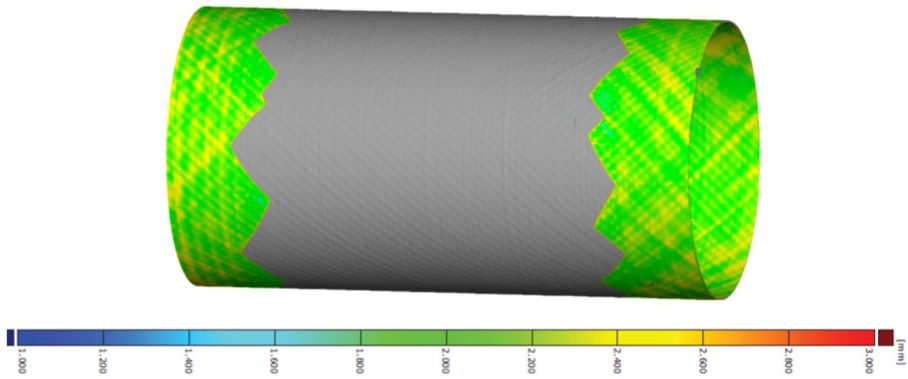


Fig. 11 Geometrical thickness scan of composite cylinder 1366

4.3 Manufacture of Metal Parts

The end-caps and outer rings were manufactured from titanium grade 5, considering the outer actual diameter of the composite cylinders and the required gap for the adhesive joint. Additive manufacturing was considered the most efficient for these thin-walled components of complex shape. In-house manufacture by Direct Energy Deposition (DED) was chosen and microscopy of cross-sections confirmed a virtually pore free material, while initial studies of samples manufactured by Powder Bed Fusion (PBF) demonstrated significant porosity. Since the geometry contains a solid block at the tip where the valves are mounted, it was decided to machine these pieces from solid titanium and use them for starting the DED-printing. In Fig. 12a the DED-printing of an end cap is shown. The printing starts on the prefabricated threaded end-piece held by the chuck.

For the thin-walled outer rings a 20 mm thick titanium plate was used for starting the printing. The plate that the ring was printed on also served as holding fixture for

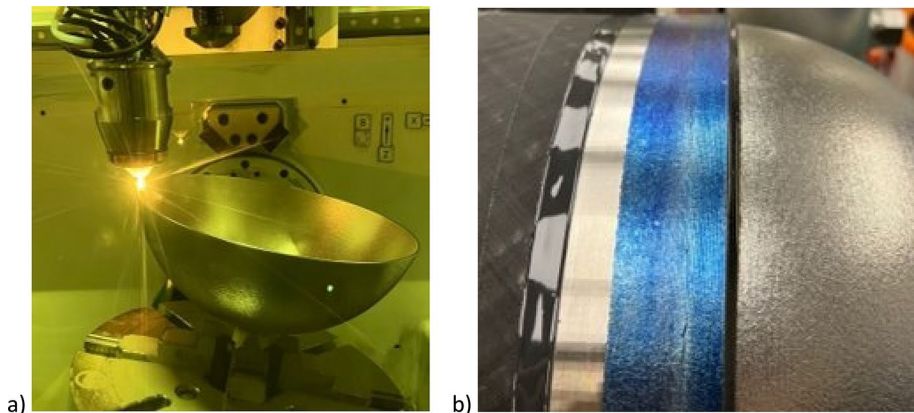


Fig. 12 **a** DED-printing of titanium grade 5 for the end caps, **b** Bonded joints between tube, end cap and outer ring. The blue colour originates from annealing prior to machining

the rings in the final machining to tolerance. It was learned that the rings required annealing in controlled atmosphere to release internal stresses prior to machining to avoid deformation.

4.4 Assembly

The assembly included bonding of end caps and outer rings at each end of the tube. Prior to bonding the surfaces were cleaned and prepared according to a procedure verified on test samples. For the titanium this included glass blasting followed by ultrasonic cleaning and finally a water based alkaline cleaning. The composite surfaces were treated with solvent cleaning and grinding. After surface treatment the lines where the joint ended on the tube and the end cap were masked, which was followed by manual application of the adhesive with a spatula on both surfaces to be bonded. The pieces were pressed together under rotation to prevent misalignment. The excess adhesive was scraped off and fillets were formed along the bond lines. Figure 12b shows the joints between tube, end cap, and outer ring after completed bonding.

To confirm a proper adhesive coverage the cured bonded joints were leak tested by vacuum testing at -0.999 Bar. Pass criterion was no detected leakage at the detection level ± 1 mbar for 20 min testing time.

Prior to the tests with internal pressure the vessels were equipped with an outer safety “cage” designed to prevent an explosive “pop-off” of the end caps in case of adhesive joint failure. The “cage” consisted of two stainless steel rings resting on the edges of the outer support rings and joined via eight threaded rods in stainless steel, as shown in Fig. 13. The locking nuts were mounted to allow axial shrinkage of the rods without imposing any axial loads during cooling.

Before being sent for testing with cryogenic content both vessels were tested with pressurised water to a pressure of 5 bar. No leaks were detected, and the total content of the

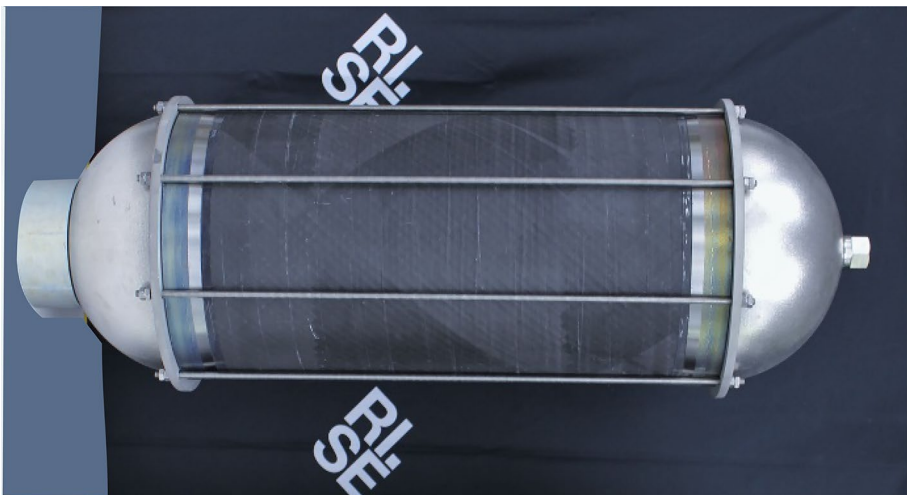


Fig. 13 Vessel ready for testing, with outer safety cage

vessel was found to be 58.2 L. After this initial test the vessels were dried for 48 h using air at 30–35 °C to avoid any generation of ice particles during transport or during the subsequent filling with liquid gas.

5 Test of Complete Vessels

5.1 Cyclic Testing

Testing of the two vessels was performed in Spain at the INTA-CEAES facilities in Cuadros (León), according to a test programme defined by RISE. Subsequent data analysis and fractography was performed at RISE. Each vessel was equipped with one strain gauge in the hoop direction and one in the axial direction at three equidistant positions along the circumference (with 120° spacing) at the middle of the tube (half-way to both ends). Furthermore, temperature sensors were placed inside the vessel at the top and at bottom. For the cyclic test, an additional temperature sensor was installed on the outside of the vessel (between the insulation and the vessel itself) as well as a scale for weighing the content. Filling and emptying were done from the bottom of the vessel, using liquid nitrogen (LN2) for cost and safety reasons.

The burst test (after successful cyclic testing) consists of filling with LN2 followed by closing the valve for limiting pressure/boil-off and subsequent monotonous temperature increase until burst, alternatively a clear leakage at 10–20 bar.

Figure 14 describes time histories for pressure, weight, temperature, and strains during the beginning (almost 5 entire cycles) of the cyclic test. The cyclic test consists of 20 cycles with a single cycle filling the vessel weight-controlled to achieve 40 kg of LN2, a dwell time to reach 4 bar gauge (differential) pressure, and emptying to 10% of remaining content weight, which

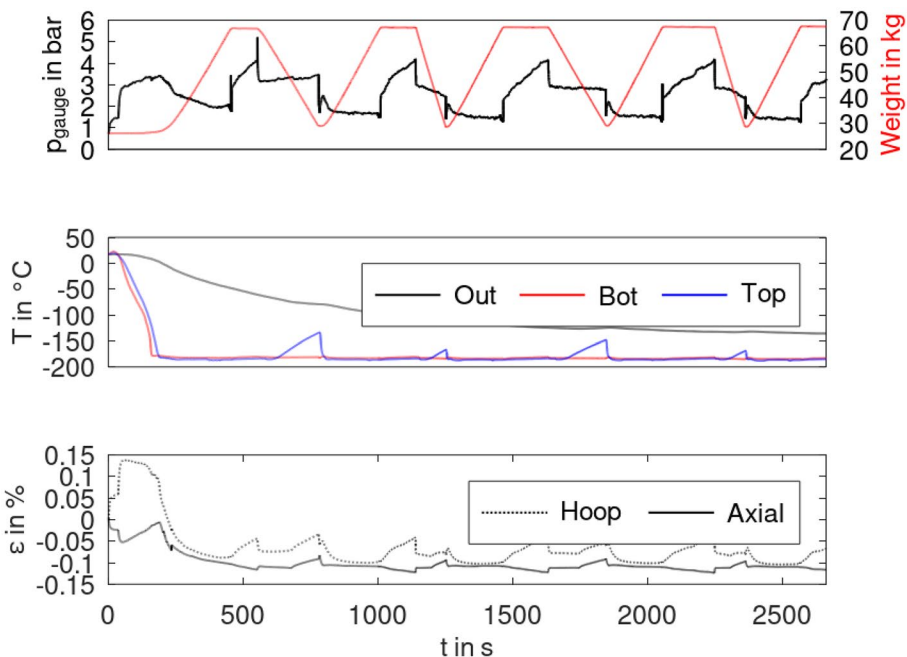


Fig. 14 Pressure, weight, temperature, and strain histories at the beginning of the cyclic test

explains the peaks at the upper temperature sensor. Since the additional temperature sensor was installed outside the vessel, between the insulation and the vessel itself, the temperature measured is higher than inside the vessel. In contrast, the CCTD programme used 20 cycles of filling with LH2 to 6.9 bar [5], while the Japanese project used a single filling with LN2 to 10 bar [6].

The evolution of the strain measurement reveals that the strain in hoop direction is proportional to pressure, whereas the axial strain is negative and inversely proportional to pressure.

Both vessels endured 20 cycles with 4 bar peaks, i.e., 14% of the burst pressure (29.4 bar), see subsequent section on burst testing, without signs of leakage or damage. Note that, for clarity, only the first cycles are shown, as the subsequent cycles were virtually identical.

5.2 Burst Test

One of the vessels (1366) was tested up to a pressure of 21.5 bar without any signs of failure or leakage, but the test was interrupted due to need to change to valves allowing a higher pressure. After changing the valve a second vessel (1365) was tested for burst. Figure 15 describes time histories for pressure and temperature at the bottom and top of the vessel during the burst test. The test cycle involves initiation of filling, which causes a pressure peak and slight temperature increase, followed by a temperature drop to $-182\text{ }^{\circ}\text{C}$, a slight temperature increase and initiation of heating of the liquid. The gas in the top of the vessel starts to heat later and eventually the vessel approaches a uniform temperature at a pressure of about 29.4 bar, corresponding to the final burst pressure. The CCTD project [5] and the Japanese project [6] did not involve burst tests, although both projects involved tests to the design pressure of 10 bar [6].

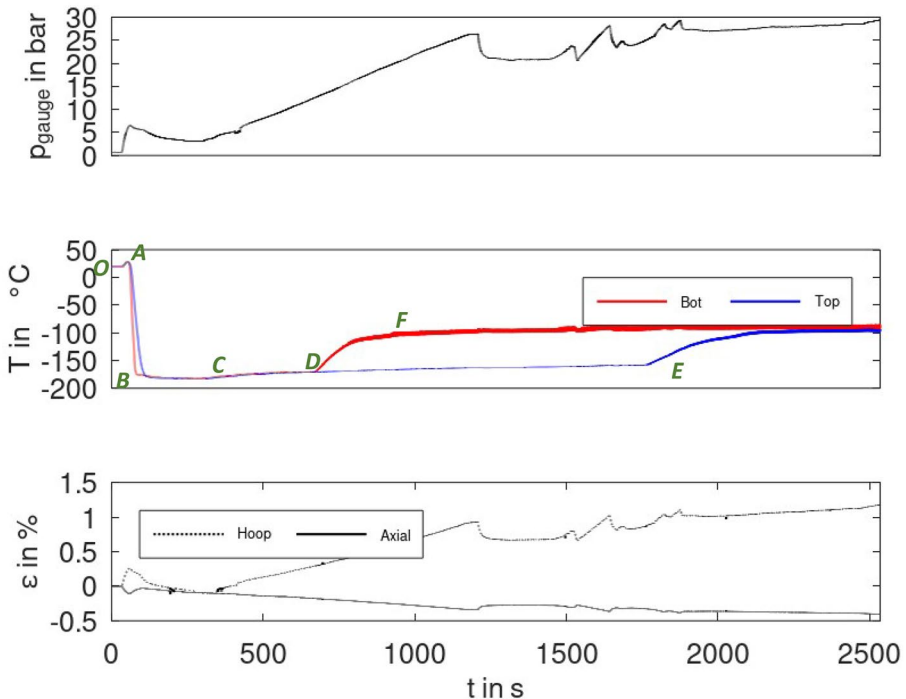
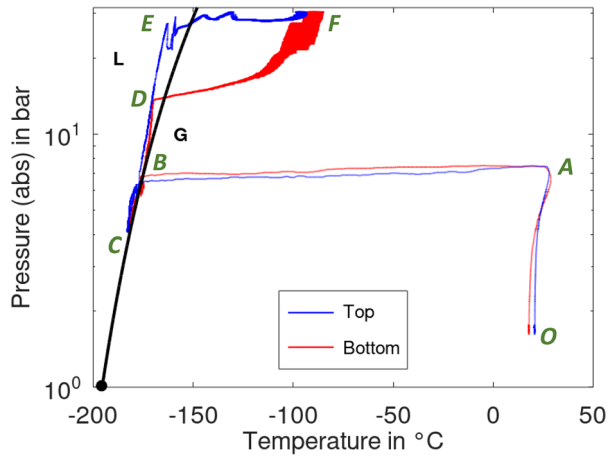


Fig. 15 Pressure, temperature, and strain histories for the burst test

Fig. 16 Pressure versus temperature cycle for nitrogen in the burst test



The lack of temperature increases in the upper gas filled part of our vessel appears to be related to an observed temporary leakage in the venting valve, which caused pressure oscillations between 1200 s and 1800 s. This results in boil-off and a corresponding loss in temperature of the gas. Once the valve was operating properly the pressure stabilised and the temperatures in the top and bottom of the vessel approached a uniform value. The phase transitions of the nitrogen in the vessel are better understood by considering a pressure-temperature diagram for the same data, as presented in Fig. 16, where “L” corresponds to liquid phase and “G” to gaseous phase.

From the evolution of strains in the hoop and axial directions, a barrelling effect can be deduced due to the increase in hoop strain and a decrease in axial strain with increasing pressure. Since the strain gauges in the hoop direction disconnected during the pressure increase phase, the inverse proportionality between hoop and axial strains was used to extrapolate the subsequent development of the hoop strain.

Figure 17a depicts the evolution of mechanical stresses in ply material coordinates, based solely on the internal pressure, deduced from the principal stresses in hoop and axial direction using transformation equations. Thereby, σ_2 represents the stress transverse to fibres and the τ_{12} shear stress, both representing the most crucial/critical stresses, with maxima $\sigma_2 = 154$ MPa and $\tau_{12} = 48.7$ MPa. Beside the stresses in the cylindrical tube section, also the average shear stress at the bond line was investigated using the axial stress in

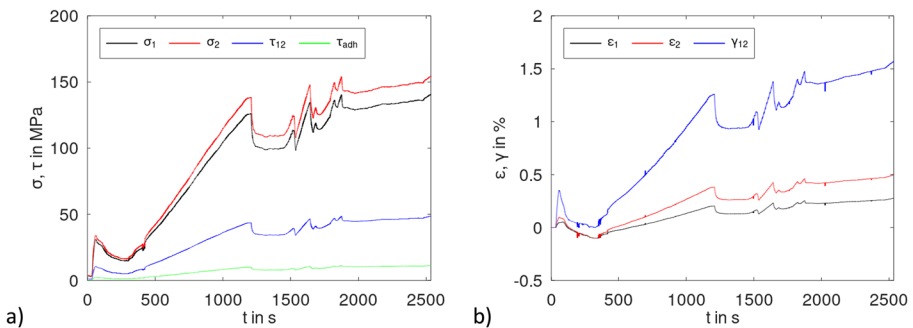


Fig. 17 Evolution of **a** mechanical stresses **b** thermo-mechanical strains

the tube and the bond length of the adhesive joint. The peak value was $\tau_{adh} = 11.2$ MPa, which is below the shear strength of 17 MPa measured in a lap shear test after ten thermal cycles to -189 °C.

Figure 17b depicts the evolution of thermo-mechanical strains in different orientations, based on the internal pressure and the thermal loading, deduced from the principal strains measured by one selected pair of strain gauges oriented in hoop and axial direction using transformation equations. The fibre transverse strain reaches a maximum of $\varepsilon_2 = 0.5\%$, and the shear strain a maximum of $\gamma_{12} = 1.6\%$.

Figure 18a depicts the scheme of the camera setup for burst testing, with camera 2 having a frame rate of 30 Hz and camera 1 having a frame rate of 60 Hz. Figure 18b, d

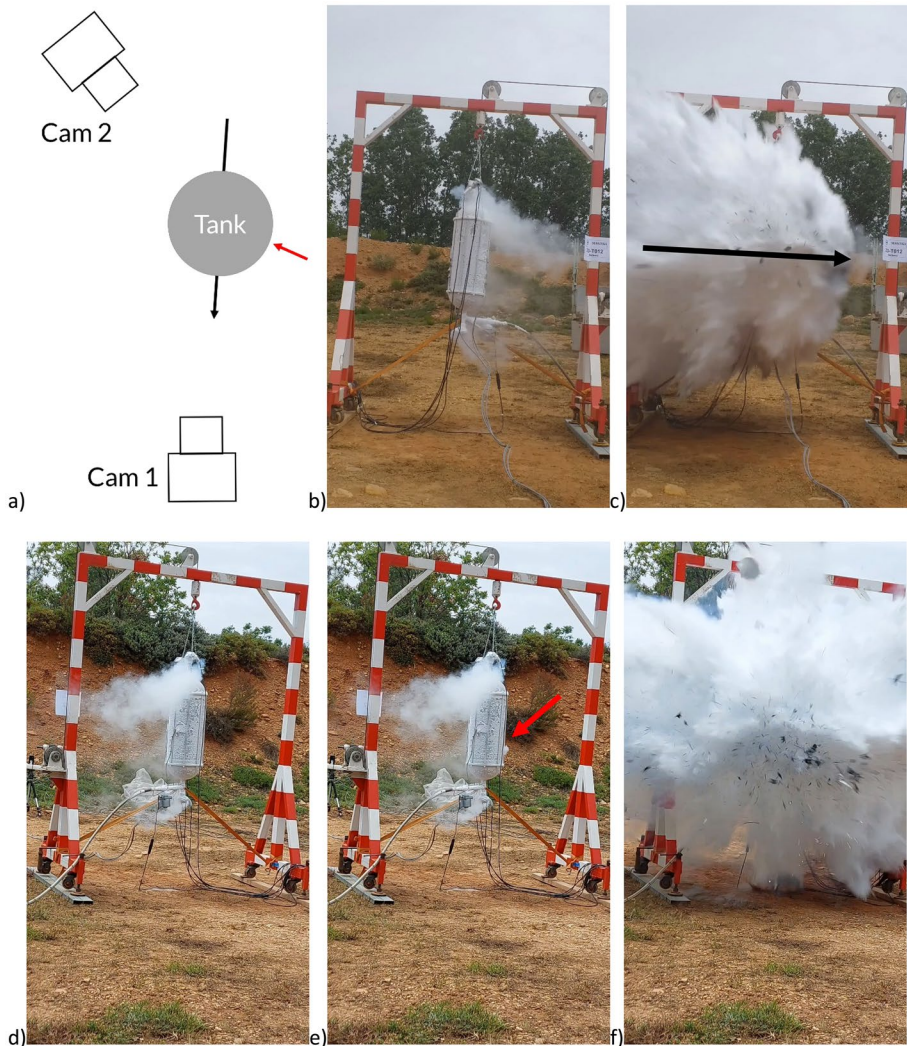


Fig. 18 a Scheme of the camera setup b Cam2 – before burst c Cam2 – +33.3 ms d Cam1 – before burst e Cam1 – before burst + 16.7 ms f Cam1 – before burst + 33.3 ms

show representative image frames extracted from the video recordings during pressure increase with no signs of damage or other anomalies.

Figure 18e depicts a leak in the lower section of the vessel, whereas Fig. 18c, f depict the burst. Note that there was no temporal synchronization between the cameras. The horizontal blast cone shown in Fig. 18c suggests a burst at the central tube section of the vessel, in direction towards camera 1, see also Fig. 18a, f. These observations indicate that failure may have initiated at some distance from the adhesive joint. This contradicts the predictions of the FE analysis, but it is also possible that failure initiated in the joint and then propagated some distance before the final catastrophic failure. Furthermore, the elastic properties and cohesive strength of the adhesive in the FE analysis are uncertain as they were extrapolated to cryogenic temperature.

Figure 19 shows a fractography of the composite tube, with the orientation of the vessel mimicking the view of camera 2, c.f. Figure 18a, but rotated 90° clockwise. The cardboard inside the cylinder hull was used to show the initial diameter (the fractured tube coiled due to internal/residual stresses) and the pieces missing. Both end caps were fractured, presumably due to impacts with the ground and the frame.

Ply stresses were calculated for the burst test using classical laminate theory. As previously, the thermomechanical loading was applied in two steps: First the thermal load was applied using the calculated thermomechanical ply properties shown in Table 1. Secondly, the mechanical load (pressure difference) was applied using the calculated material properties at -100 °C, which was the measured temperature at the end of the burst test. Figure 20 shows the ply stress components vs applied pressure. At failure (burst) the transverse tensile stress in the plies is about 97 MPa, and the shear stress about 68 MPa, which should be compared with the predicted in-situ strengths of 108 MPa and 182 MPa for a surface ply, see Table 1.

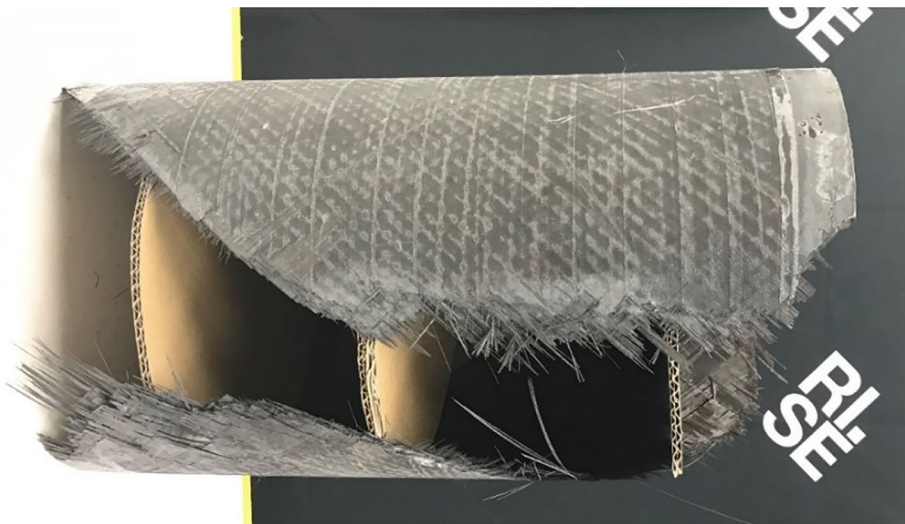


Fig. 19 Fractographic investigation on the debris of the cylinder

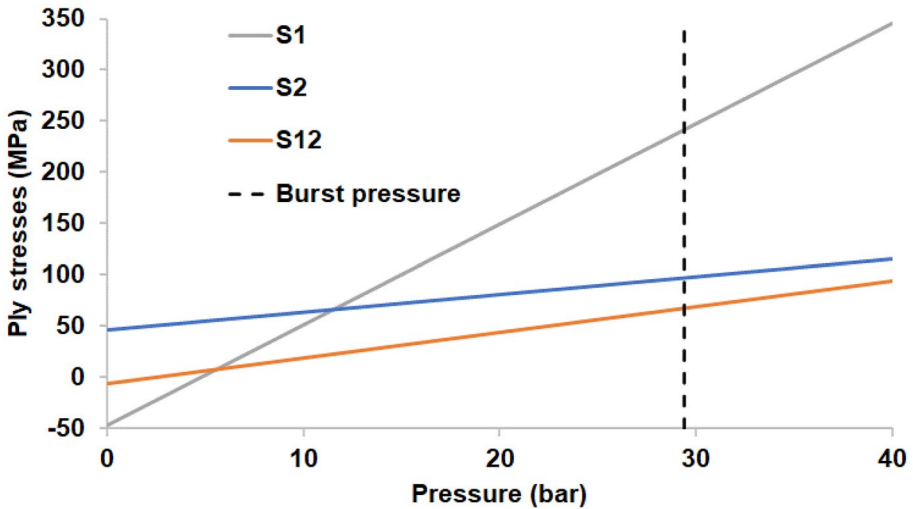


Fig. 20 Predicted ply stresses in the $\pm 41^\circ$ cylinder for a constant temperature of -100°C

6 Implications for Future Design and Development

Using stainless steel with an ultimate stress of 344 MPa (at cryogenic conditions) requires a thickness of 1.2 mm to sustain a burst pressure of 30 bar. The mass of an all-steel vessel would be 8.0 kg, including 4.8 kg of the cylinder and 3.2 kg for the two end caps. The mass of the current vessel (excluding the “safety cage”) was 6.2 kg, including 1.9 kg of the composite cylinder and 4.3 kg for the two end caps with outer rings. Thus, the composite cylinder was 60% lighter than a steel cylinder. Also note that the titanium end caps were not designed for minimum weight, but for the minimum thickness that could be manufactured by available additive manufacturing, while serial production would involve pressing of sheet metal with optimised thickness. Future tanks may be designed either as a composite cylinder with end caps in metal (as in the current case), or as an all-composite tank.

The advantage of metal end caps is that they can be produced as a standard component for tanks of different length and volume, which offers significant design flexibility, where the weight savings of using a composite cylinder increase for longer tanks. Furthermore, metal end caps allow threading and simple connection of sensors, valves, and pipes. Finally, they provide the preferred in-plane isotropy and may be produced with small thickness and in locally complex shapes. The drawbacks are the need for an adhesive joint, a higher specific weight, and challenges in matching thermal strains. In the present design thermal hoop strains were matched by deviating from the optimal layup for strength of the composite cylinder.

The most obvious advantages of an all-composite tank are a potential for lower weight and minimization of thermal strains due to more similar CTEs. There will, however, always be some thermal strains associated with difference in layup of the cylindrical and hemispherical parts of the tank. Apart from small local bending stresses, the hemispherical parts will experience a uniform stress state where a quasi-isotropic layup of uniform thickness is preferable. A doubly curved quasi-isotropic laminate is probably best produced from a preform with discontinuous fibres, while the cylinder may be made by filament

winding or rolling of a cross-ply weave with different number of fibres in the hoop and axial directions.

Ideally the different composite sections should be co-cured, but different manufacturing procedures may require use of adhesive joints between the sections. Future use of adhesive joints requires more thorough studies of CTE, strengths and stiffness of adhesives under cryogenic conditions.

Another challenge is to develop experimental methods to determine in-situ strength of thin-ply composites under cryogenic conditions. Experiments to study crack initiation after cryogenic loading of cross-ply laminates have been done within this project and will be reported in a separate paper. Ideally this effort should be complemented by development of methods to determine intralaminar toughness under cryogenic conditions, to allow theoretical predictions of the in-situ strength.

The budget in this research project constrained testing of the vessels to 20 cycles. This is clearly insufficient for proving a design life of 20000 cycles, which would be required before commercialisation, but still allowed detection of phenomena beyond the first few cycles.

Design of real tanks also requires better understanding of the interaction and integration with supporting systems for insulation, fuelling, control of temperature and pressure, as well as a judicious definition of design loads and required safety factors, considering property variations of all materials involved.

7 Conclusions

In this project we have studied a pressure vessel involving a composite cylinder and metal end-caps with the aim to demonstrate the linerless design concept for future all-composite inner vessels for storage of liquid hydrogen. Based on previous material tests at room temperature and at the temperature of liquid hydrogen we have

- (a) Designed a lightweight linerless inner vessel based on a thin-ply polymer composite cylinder bonded to titanium end caps, considering the internal pressure and thermal stresses caused by filling with liquid hydrogen, for a design pressure of 10 bar.
- (b) Manufactured the vessel by filament wet winding of the composite cylinder and additive manufacture of the titanium end-caps and joined them by adhesive bonding.
- (c) Tested the vessel by cyclic filling and emptying with liquid nitrogen to the expected service pressure of 4 bar without any detected leakage or degradation, followed by a burst test where the vessel reached 30 bar, i.e. three times the design pressure.
- (d) The weight of the composite cylinder was 40% of a corresponding cylinder in stainless steel.

Acknowledgements The assistance with material and input on design requirements from Oxeon AB is gratefully acknowledged. Particular thanks to the lab and design staff at RISE, including Runar Långström (filament winding and specimen manufacture), Olof Säfvenberg (CAD design of joints and end caps), Kenneth Strand (Atos geometry measurements), and Henrik Dykhoff (assembly, bonding and fractography). Finally, thanks to Oscar González Espasandín, Emilio Llano Lago, and Julio Rodrigo Ruiz at INTA León in Spain, who performed testing of the vessels.

Author Contributions All authors at RISE contributed to the writing with focus on their specific work. R.O. coordinated the project, outlined and edited the manuscript, and wrote Sections 1, 2.1, 3.1, 6, and 7. C.C. performed the FE analysis and wrote Section 3.3. F.M. provided material and advice on material selection and manufacture. E.M. estimated corrected material data, performed analytical stress analysis, and wrote

Sections 2.2, 3.2 and the last paragraph of 5.2. M.M. compiled and evaluated test data and wrote Section 5. J.P. coordinated manufacture and wrote Section 4 in collaboration with R.O.

Funding Open access funding provided by RISE Research Institutes of Sweden. This work was to 92% funded by Energimyndigheten (the Swedish Energy Agency) through contract P2021-90061. Co-funding was provided by Oxeon AB. Finalisation of the manuscript has subsequently been funded by the internal development funds of RISE and Energimyndigheten (the Swedish Energy Agency) through contract P2021-90268 via the Competence Centre TechForH2.

Data Availability Data sets generated during the current study are available from the corresponding author on reasonable request.

Declarations

Ethical Approval Not applicable.

Competing Interests The authors declare no competing interests.

Open Access This article is licensed under a Creative Commons Attribution 4.0 International License, which permits use, sharing, adaptation, distribution and reproduction in any medium or format, as long as you give appropriate credit to the original author(s) and the source, provide a link to the Creative Commons licence, and indicate if changes were made. The images or other third party material in this article are included in the article's Creative Commons licence, unless indicated otherwise in a credit line to the material. If material is not included in the article's Creative Commons licence and your intended use is not permitted by statutory regulation or exceeds the permitted use, you will need to obtain permission directly from the copyright holder. To view a copy of this licence, visit <http://creativecommons.org/licenses/by/4.0/>.

References

1. Sloop, J.L.: Liquid hydrogen as a propulsion fuel, 1945–1959. NASA SP-4404. NASA, Washington DC (1978). <https://ntrs.nasa.gov/api/citations/19980019295/downloads/19980019295.pdf>
2. Air, A., Shamsuddoha, M., Prusty, B.G.: A review of Type V composite pressure vessels and automated fibre placement based manufacturing. *Compos. B* **253**, 1110573 (2023). <https://doi.org/10.1016/j.compositesb.2023.110573>
3. Zheng, H., Zeng, H., Zhang, J., Sun, H.: The application of carbon fiber composites in cryotank. In: Ares, A.E. (ed.) Ch. 5 in solidification. IntechOpen (2018). <https://doi.org/10.5772/intechopen.73127>. <https://www.intechopen.com/chapters/58970>
4. Liu, N., Ma, B., Liu, F., Huang, W., Xu, B., Qu, L., Yang, Y.: Progress in research on composite cryogenic propellant tank for large aerospace vehicles. *Compos. A* **143**, 106297 (2021). <https://doi.org/10.1016/j.compositesa.2021.106297>
5. McCarville, D.A., Guzman, J.C., Dillon, A.K., Jackson, J.R., Birkland, J.O.: Design, manufacture and test of cryotank components. In: Comprehensive composite materials II, 2nd edn. Elsevier, Amsterdam Netherlands (2018). <https://doi.org/10.1016/B978-0-12-803581-8.09958-6>
6. Morimoto, T., Ishikawa, T., Yokozeki, T., Hayashi, Y., Shimoda, T., Morino, Y.: Pressurization test on CFRP liner-less tanks at liquefied nitrogen temperature. *Adv. Compos. Mater.* **13**, 81–88 (2004). <https://doi.org/10.1163/1568551041718062>
7. Dvorak, G.J., Laws, N.: Analysis of progressive cracking in composite laminates II. First ply failure. *J Compos Mater.* **21**, 309–329 (1987). <https://doi.org/10.1177/002199838702100402>
8. Camanho, P.P., Dávila, C.G., Pinho, S.T., Iannucci, L., Robinson, P.: Prediction of in situ strengths and matrix cracking in composites under transverse tension and in-plane shear. *Compos. A* **37**, 165–176 (2006). <https://doi.org/10.1016/j.compositesa.2005.04.023>
9. Olsson, R.: In-situ strength of composite plies – theory and experiments. TR12-001. Swerea SICOMP AB, Mölndal (2012). https://www.researchgate.net/publication/349694177_In-situ_strength_of_composite_plies_-_theory_and_experiments
10. Amacher, R., Cugnoni, J., Botsis, J., Sorensen, L., Smith, W., Dransfeld, C.: Thin ply composites: experimental characterization and modeling of size-effects. *Compos. Sci. Technol.* **101**, 121–132 (2014). <https://doi.org/10.1016/j.compscitech.2014.06.027>

11. Cugnoni, J., Amacher, R., Kohler, S., Brunner, J., Kramer, E., Dransfeld, C., Smith, W., Scobbie, K., Sorensen, L., Botsis, J.: Towards aerospace thin-ply composites: effect of ply thickness, fibre, matrix and interlayer toughening on strength and damage tolerance. *Compos. Sci. Technol.* **168**, 467–477 (2018). <https://doi.org/10.1016/j.compscitech.2018.08.037>
12. Marklund, E., Asp, L.E., Olsson, R., Ohlsson, F., Varna, J.: Experimental investigation and modeling of thin band woven composites. *TexComp-11*. Leuven, 2013. “Asp TexComp 11 paper.pdf”. <https://www.mtm.kuleuven.be/english/research/scalint/cmgevents/CompositesWeek/program/papers/19-20-09-thursday-friday-texcomp-11.zip>
13. Sippel, M., Kopp, A., Mattsson, D., Freund, J., Tapeinos, I., Koussios, S.: Final results of advanced cryo-tanks research project CHATT. 6th European Conf. for Aeronautics and Space Sciences (EUCASS) (2015). <https://core.ac.uk/download/pdf/31022252.pdf>
14. Katsivalis, I., Singorini, V., Ohlsson, F., Langhammer, C., Minelli, C., Asp, L.E.: Hydrogen permeability of thin-ply composites after mechanical loading. *Compos. A* **176**, 107867 (2024). <https://doi.org/10.1016/j.compositesa.2023.107867>
15. Merzkirch, M., Marklund, E., Olsson, R., Ramantani, D.: Mechanical characterization at room and cryogenic temperature of thin-ply CFRP laminates manufactured by filament winding. Submitted for publication. (2023)
16. 3M.: Scotch-Weld™ Epoxy Adhesive 2216 B/A. Technical data 2018. 3M Industrial Adhesives and Tapes Division, St Paul MN, USA (2018). <https://multimedia.3m.com/mws/media/153955O/3mtm-scotch-weldtm-epoxy-adhesive-2216-b-a.pdf>
17. Marquardt, E.D., Le, J.P., Radebaugh, R.: Cryogenic material properties database. Proc of the 11th International Cryocooler Conference, June 20–22, 2000, Keystone, CO. https://trc.nist.gov/cryogenics/Papers/Material_Properties/2000-Cryogenic_Material_Properties_Database.pdf
18. Sapi, Z., Butler, R.: Properties of cryogenic and low temperature composite materials – a review. *Cryogenics* **111**, 103190 (2020). <https://doi.org/10.1016/j.cryogenics.2020.103190>
19. Hohe, J., Neubrand, A., Fliegner, S., Beckmann, C., Schober, M., Weiss, W.P., Appel, S.: Performance of fiber reinforced materials under cryogenic conditions - a review. *Compos. A* **141**, 106226 (2021). <https://doi.org/10.1016/j.compositesa.2020.106226>

Publisher’s Note Springer Nature remains neutral with regard to jurisdictional claims in published maps and institutional affiliations.